# The effects of electron energy distribution and ionization cross section uncertainty on charge breeder ion source diagnostics with pulsed 1+ injection

M. Luntinen, J. Angot, H. Koivisto, O. Tarvainen, T. Thuillier, and V. Toivanen

**Published version information**

**Citation:** M Luntinen et al. The effects of electron energy distribution and ionization cross section uncertainty on charge breeder ion source diagnostics with pulsed 1+ injection. Phys Plasmas 30, no. 7 (2023): 073904

**DOI:** 10.1063/5.0150198

RESEARCH ARTICLE | JULY 18 2023

# The effects of electron energy distribution and ionization cross section uncertainty on charge breeder ion source diagnostics with pulsed 1+ injection

M. Luntinen ; J. Angot ; H. Koivisto ; O. Tarvainen ; T. Thuillier ; V. Toivanen



*Phys. Plasmas* 30, 073904 (2023)
https://doi.org/10.1063/5.0150198

Physics of Plasmas ARTICLE pubs.aip.org/aip/pop

# The effects of electron energy distribution and ionization cross section uncertainty on charge breeder ion source diagnostics with pulsed 1+ injection

Cite as: Phys. Plasmas **30**, 073904 (2023); doi: 10.1063/5.0150198
Submitted: 13 March 2023 · Accepted: 2 June 2023 ·
Published Online: 18 July 2023



M. Luntinen,[1,a)] J. Angot,[2] H. Koivisto,[1] O. Tarvainen,[3] T. Thuillier,[2] and V. Toivanen[1]

## AFFILIATIONS

[1]Accelerator Laboratory, Department of Physics, University of Jyväskylä, FI-40014 Jyväskylä, Finland
[2]Université Grenoble Alpes, CNRS, Grenoble INP, LPSC-IN2P3, 38000 Grenoble, France
[3]UK Science and Technology Facilities Council, ISIS Pulsed Spallation Neutron and Muon Facility, Rutherford Appleton Laboratory, Harwell Campus, Didcot OX11 0QX, United Kingdom

[a)]**Author to whom correspondence should be addressed:** miha.s.p.luntinen@jyu.fi

## ABSTRACT

The consecutive transients (CT) method is a plasma diagnostic technique of charge breeder electron cyclotron resonance ion source plasmas. It is based on the short-pulse injection of singly charged ions and the measurement of the resulting transients of the extracted multi-charged ion beams. Here, we study the origin of the large uncertainty bounds yielded by the method to reveal avenues to improve its accuracy. We investigate effects of the assumed electron energy distribution (EED) and the uncertainty inherited from the ionization cross section data of $K^{4+}$–$K^{12+}$ ions on the resulting plasma electron density $n_e$, average energy $\langle E_e \rangle$, and the characteristic times of ion confinement $\tau^q$, electron impact ionization $\tau^q_{\mathrm{inz}}$, and charge exchange $\tau^q_{\mathrm{cx}}$ provided by the CT method. The role of the EED was probed with Kappa and double-Maxwellian distributions, the latter resulting in a shift of the $n_e$ and $\langle E_e \rangle$ distributions. The uncertainty of the ionization cross section $\sigma^{\mathrm{inz}}_{q\to q+1}$ was artificially curtailed to investigate its impact on values and uncertainties of the plasma parameters. It is demonstrated that the hypothetical perfect knowledge of $\sigma^{\mathrm{inz}}_{q\to q+1}$ significantly reduces the uncertainties of $\tau^q$, $\tau^q_{\mathrm{inz}}$, and $\tau^q_{\mathrm{cx}}$, which motivates the need for improved cross section data.





## I. INTRODUCTION

Electron cyclotron resonance ion sources (ECRIS)[1] are used worldwide for the production of stable, high intensity beams of medium to high charge state ions for the purpose of accelerator based nuclear physics,[2,3] heavy ion based radiotherapy,[4,5] and various industrial applications (e.g., Refs. 6 and 7). ECRIS operation is based on the magnetic confinement and microwave heating of electrons, which breakup and ionize neutral gas supplied into the plasma chamber at near vacuum pressure.

ECRIS based charge breeders[8] are a vital component of ISOL facilities exploring the boundaries of the nuclear chart. They enable efficient conversion of the low intensity 1+ beam of rare and short-lived isotopes to high charge state ions required for post-acceleration. Due to the diminishing reaction cross sections involved in the nuclear physics experiments (i.e., production of the heavy isotopes), ever greater beam intensities are demanded. As the 1+ intensities yielded by the ISOL method are typically low, the charge breeder efficiency needs to be as high as possible to realize this. Fundamental nuclear physics research, hence, benefits from the continued improvements in ECRIS technology, which in turn requires the development of state-of-the-art plasma diagnostics methods for R&D purposes and benchmarking of simulations.[9–11]

One of the keys to ECRIS development for charge breeding lies in optimizing the electron density $n_e$ and average energy $\langle E_e \rangle$ in the plasma. These parameters affect directly the rate of ionization—a higher electron density implies more collisions, and a higher impact energy enables higher charge states to be produced. The electron density and energy also modify the ion confinement properties. The energetic electrons also experience improved confinement within the minimum-$B$ structure of the ECRIS magnetic field. This leads to a

buildup of a hot electron component in the plasma core, which causes a negative potential dip $\Delta\Phi$ in the otherwise positive plasma potential profile $\Phi$.[1,12,13] This dip presents an electrostatic barrier to the positive highly charged ions in the central plasma, improving their confinement. The electron energy distribution (EED) of ECR ion sources has been studied, e.g., using escaping electron spectroscopy,[14,15] while singly charged ion beam injection,[16,17] microwave interferometry,[18] and bremsstrahlung emissions[19] can be used for studying the electron density. On the other hand, plasma diamagnetism[20,21] diagnostic yields information on the plasma energy content $n_e\langle E_e\rangle$.

Decreasing charge exchange rate between ions and neutral atoms also leads to improvements in the charge breeding efficiency of high charge states. Here, the ion captures a valence electron from the valence orbital of the neutral atom, leading to a decrease in its charge state. Charge exchange can be counteracted by decreasing the neutral density, i.e., decreasing the input of the neutral gas and hence the pressure, or by using a gas with a high first ionization potential.

The characteristic times of ion confinement, ionization, and charge exchange ($\tau^q$, $\tau^q_{\text{inz}}$, and $\tau^q_{\text{cx}}$, respectively) are measures for their respective processes. These have been probed by means of beam current transient measurements,[22–26] which are based on the modeling of the beam current through the balance equation of ion densities. The consecutive transients (CT) method discussed in this work is the latest improvement in this lineage of diagnostics methods. The major improvements over the previous techniques are that (i) the CT method requires fewer assumptions—in particular, no assumptions need to be made regarding the functional dependence of the confinement time on the ion charge state—and (ii) while the previous methods equate the in-plasma ion density to the extracted beam current (i.e., $qn^q \propto I^q$), the CT method incorporates the confinement time dependence (i.e., $I^q \propto qn^q/\tau^q$) similar to Ref. 25.

We have shown[27–29] that the consecutive transients method (CT) can be used to obtain postdictions for $n_e$, $\langle E_e\rangle$, $\tau^q$, $\tau^q_{\text{inz}}$, and $\tau^q_{\text{cx}}$ with a parsimony of assumptions. The working principle of the CT method is recounted in Sec. II. The downside of the technique is the considerable uncertainty associated with the results, e.g., for the confinement time of potassium $\tau^{8+}_{\text{K}} = 14.4^{+23.1}_{-5.9}$ ms or an uncertainty of 200% (see Table IV). We investigate here the method's intrinsic uncertainty originating from parameters, which need to be either assumed or taken from the literature, as opposed to the uncertainty involved with the experimental setup, such as the perturbation caused on the support plasma or the source tuning error due to, e.g., hysteresis of the yoke magnetic material. The study of the effect of the intrinsic error sources is critical, as they are beyond the control of the experimenter and play a deciding role in the estimation of the robustness of the method.

Two sources of uncertainty are computationally relevant: (1) The method requires the user to presume a certain EED, which is used to evaluate the ionization rate coefficients, thus affecting the resulting $n_e$ and $\langle E_e\rangle$ values. In Sec. III A, we probe the sensitivity of the method to the EED with a particular focus on the high-energy tail of the presumed distribution; (2) the electron impact rate coefficients are computed using literature values of the cross sections, some of which are subject to considerable experimental uncertainty [for example, the cross section of the ground state electron-impact ionization of $K^{8+}$ to $K^{9+}$, $\sigma^{\text{inz, K}}_{8+\to 9+}$, carries a reported relative uncertainty of 200% (Ref. 30)]. In the absence of more precise literature values, we investigate here the effect of arbitrary curtailing the uncertainty limits to simulate more precise knowledge of the cross sections (Sec. III B). In short, the purpose of this work is to establish what is the effect of varying the presumed EED on the method results, and whether or not more precise cross section data could lead to an improvement in the result precision.

## II. THE CT METHOD

The experimental methodology of the CT method is illustrated schematically in Fig. 1. Short ($\lesssim$10 ms) pulses of 1+ ions of a probe element (metallic, to minimize wall recycling effects) are injected into a support gas plasma sustained within the ECRIS. The injected ions are captured by the plasma where they experience ionization by electron-impact and charge exchange with neutral atoms, until escaping confinement. A portion of the escaped ions form the N+ beam, i.e., the extracted beam comprised of the various charge states' ions. The N+ beam is $m/q$ analyzed using a dipole magnet, and the beam transient time series of consecutive charge states (minimum of 5) are measured with a Faraday cup.

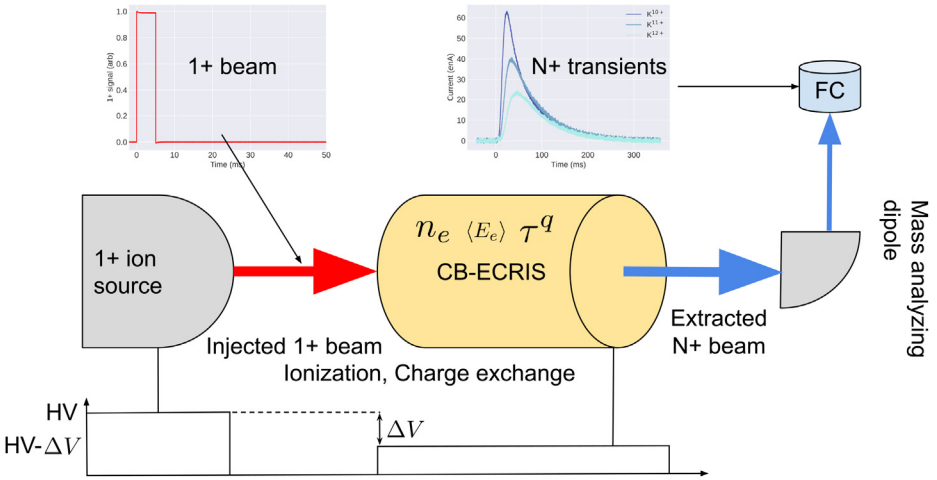


FIG. 1. The experimental principle of the consecutive transients method.

### A. Analysis procedures

The time evolution of the plasma charge state distribution (CSD) of the injected material is described by the balance equation,[12]

$$\frac{dn^q}{dt} = +n_e\langle\sigma v\rangle^{\text{inz}}_{q-1\to q}n^{q-1} - n_e\langle\sigma v\rangle^{\text{inz}}_{q\to q+1}n^q + n_0\langle\sigma v\rangle^{\text{cx}}_{q+1\to q}n^{q+1} - n_0\langle\sigma v\rangle^{\text{cx}}_{q\to q-1}n^q - n^q/\tau^q, \quad (1)$$

where $\langle\sigma v\rangle^{\text{inz/cx}}$ is the rate coefficients of ionization/charge exchange. Here, it is assumed that electron impact ionization dominates over photoionization and double (and other higher order) ionization reactions have been omitted. Charge exchange takes place with neutral atoms of the support plasma (density $n_0$). Ion–ion charge exchange is neglected as it becomes increasingly unlike with $q$ due to the increasing ionization potentials[31–33] and the Coulomb repulsion between like-charged ions. Furthermore, the balance equation assumes that owing to their high collisionality, the ions are in Maxwellian thermal equilibrium. The term $-n^q/\tau^q$ defines the $n^q$ population confinement time $\tau^q$ through diffusive processes, i.e., ion losses caused by instabilities are ignored. The ionization and charge exchange times are defined through the corresponding rates,

$$\tau^q_{\text{inz}} = \left(n_e\langle\sigma v\rangle^{\text{inz}}_{q\to q+1}\right)^{-1} \quad (2)$$

and

$$\tau^q_{\text{cx}} = \left(n_0\langle\sigma v\rangle^{\text{cx}}_{q\to q-1}\right)^{-1}. \quad (3)$$

We combine the balance equation with a model for the extracted beam current,[27,34,35]

$$I^q = \kappa F_B L S\frac{n^q q e}{\tau^q}, \quad (4)$$

where $\kappa$, $L$, and $S$ are the beamline transmission efficiency, length of the plasma, and area of the extraction aperture, respectively. For generality, we have introduced the mirror ratio dependent factor $F_B$ that determines the fraction of the ions escaping confinement that are lost toward the extraction. The $\kappa$, $F_B$, $L$, $S$, and elementary charge $e$ cancel out upon substitution in Eq. (1), giving us the time evolution of the extracted and detected beam as

$$\dot{I}^q = a_q I^{q-1} - b_q I^q + c_q I^{q+1}, \quad (5)$$

where

$$a_q = n_e\langle\sigma v\rangle^{\text{inz}}_{q-1\to q}\frac{q}{q-1}\frac{\tau^{q-1}}{\tau^q}, \quad (6)$$

$$b_q = \left(n_e\langle\sigma v\rangle^{\text{inz}}_{q\to q+1} + n_0\langle\sigma v\rangle^{\text{cx}}_{q\to q-1} + 1/\tau^q\right), \quad (7)$$

$$c_q = n_0\langle\sigma v\rangle^{\text{cx}}_{q+1\to q}\frac{q}{q+1}\frac{\tau^{q+1}}{\tau^q}. \quad (8)$$

Fitting Eq. (5) to the measured time series data, the coefficients $a_q$, $b_q$, and $c_q$ are obtained as the fitting parameters. It is emphasized that these coefficients are not affected by the uncertainties of the ionization or charge exchange cross sections, but merely carry the uncertainty associated with the fitting procedure, which contributes to the uncertainty of the results only when the signal-to-noise ratio of the data is poor. By algebraic manipulation, it is possible to construct an equation depending only on the coefficients $a_q$, $b_q$, $c_q$, and $n_e$ and $\langle E_e\rangle$,

$$\frac{q}{q+1}\frac{a_{q+1}}{n_e\langle\sigma v\rangle^{\text{inz}}_{q\to q+1}} = \frac{b_{q+1} - n_e\langle\sigma v\rangle^{\text{inz}}_{q+1\to q+2} - \dfrac{a_{q+1}c_q}{n_e\langle\sigma v\rangle^{\text{inz}}_{q\to q+1}}}{b_q - n_e\langle\sigma v\rangle^{\text{inz}}_{q\to q+1} - \dfrac{a_q c_{q-1}}{n_e\langle\sigma v\rangle^{\text{inz}}_{q-1\to q}}}. \quad (9)$$

Solving Eq. (9) requires the parameters $a_q$, $a_{q+1}$, $b_q$, $b_{q+1}$, $c_{q-1}$, and $c_q$, which dictates that the transients of five consecutive charge states must be measured.

Equation (9) has an infinitude of solutions, and the acceptable solution set is obtained by defining a penalty function,

$$F^q(n_e, \langle E_e\rangle) = \left|\frac{q}{q+1}\frac{a_{q+1}}{n_e\langle\sigma v\rangle^{\text{inz}}_{q\to q+1}} - \frac{b_{q+1} - n_e\langle\sigma v\rangle^{\text{inz}}_{q+1\to q+2} - \dfrac{a_{q+1}c_q}{n_e\langle\sigma v\rangle^{\text{inz}}_{q\to q+1}}}{b_q - n_e\langle\sigma v\rangle^{\text{inz}}_{q\to q+1} - \dfrac{a_q c_{q-1}}{n_e\langle\sigma v\rangle^{\text{inz}}_{q-1\to q}}}\right| \Bigg/ \frac{q}{q+1}\frac{a_{q+1}}{n_e\langle\sigma v\rangle^{\text{inz}}_{q\to q+1}}, \quad (10)$$

and minimizing it as a function of $\langle E_e\rangle$ in a dense array of $n_e$ points. Here, the dependence on $\langle E_e\rangle$ comes from the ionization rate coefficients, defined as

$$\langle\sigma v\rangle^{\text{inz}}_{q\to q+1} = \int_0^\infty g(v;\langle E_e\rangle)\sigma^{\text{inz}}_{q\to q+1}(v)v\,dv, \quad (11)$$

where $g(v;\langle E_e\rangle)$ is the EED as a function of speed and parameterized by the average energy of the distribution. Strictly speaking $v$ is the relative speed of the electrons and ions, but owing to the much smaller mass and greater energy of the electrons, the ions can be considered stationary. The $\sigma^{\text{inz}}_{q\to q+1}$ of potassium in our work is taken from the literature values for the ground state electron-impact ionization reported in Refs. 30 and 36. The upper limit of $F$ is selected to be low enough that each solution set contains on the order of $10^3$ solutions for sufficient statistics. In this work, we set $F \le 10^{-6}$. The effect of restricting the upper limit of $F$ is elaborated in Appendix A.

The solution sets depend on the EED presumed in the calculation of the rate coefficients $\langle\sigma v\rangle^{\text{inz}}$. Since the rate coefficients directly inherit the experimental uncertainty carried by $\sigma^{\text{inz}}_{q\to q+1}$, as can be seen from Eq. (11), this is reflected in the uncertainty of the method results.

The characteristic times can then be computed within the solution set according to[37]

$$\tau^q = \left(b_q - n_e\langle\sigma v\rangle^{\text{inz}}_{q\to q+1} - \frac{a_q c_{q-1}}{n_e\langle\sigma v\rangle^{\text{inz}}_{q-1\to q}}\right)^{-1}, \quad (12)$$

$$\tau^q_{\text{cx}} = \left(b_q - n_e\langle\sigma v\rangle^{\text{inz}}_{q\to q+1} - 1/\tau^q\right)^{-1}, \quad (13)$$

and

$$\tau^q_{\text{inz}} = 1/n_e\langle\sigma v\rangle^{\text{inz}}_{q\to q+1}. \quad (14)$$

We eliminate unphysical results by demanding that the characteristic times are positive. As we obtain a set of solutions for $\langle E_e\rangle$ and $n_e$, we

obtain also a distribution for $\tau^q$, $\tau^q_{cx}$, and $\tau^q_{inz}$. To plot the results, we take the median value between the upper and lower uncertainty limits so that they enclose 34.1% of all solutions, respectively (reflecting a one sigma confidence interval for a Gaussian distribution).

In this work, the determination of the coefficients $a_q$, $b_q$, and $c_q$ was conducted by solving Eq. (5) with a fourth-order Runge–Kutta method using a time step of $10^{-4}$ s and minimizing the least squares difference between the measured time series for $I^q$ and the numerical solution. The $\langle E_e \rangle$, $n_e$ optimization (i.e., the minimization of the penalty function), was performed in a 1000 element array of logarithmically spaced $n_e$ values, and 1000 Monte Carlo (MC) iterations for the uncertainty were performed. A small random displacement was added to the elements in the $n_e$ array between each MC iteration to better cover the search space.

### B. Experimental data

The data analyzed in this work are from the experimental campaign conducted for Ref. 27 on the 14.5 GHz CB-ECRIS at the LPSC. The relevant source operating parameters are summarized in Table I. The corresponding characteristic times and charge breeding efficiencies of potassium in helium plasma are tabulated in Table II. Singly charged potassium ions were injected in 10 ms pulses into a helium support plasma sustained within the ECRIS. The N+ beam was mass analyzed using a dipole magnet, and the transient time series were collected at the N+ Faraday cup. The experimental setup and methods are discussed in detail in Ref. 27.

The key results of Ref. 27 can be summarized as follows: We showed that the method can be used to obtain postdictions for the electron density and average energy, i.e., the energy content of the plasma, as well as the characteristic times; the closed electron shell of $K^{9+}$ is visible in the ionization times; the charge exchange time exhibits a minimum at $K^{8+}$ from which it was inferred that although the cross section of charge exchange increases with the charge state, the decreasing neutral density toward the plasma core mitigates its effects for high charge states; the confinement time was found to satisfy a power law within the uncertainty bounds, with the long confinement times of the high charge states implying that at the charge breeder ECRIS plasma conditions the highly charged ions are indeed electrostatically confined with the low charge states being magnetized; the energy content $n_e\langle E_e \rangle$ was found to be constant as a function of charge state (within the uncertainty limits), and the plasma triple product $n_e\langle E_e \rangle \tau^q$ was seen to increase with $q$—in agreement with the Golovanivsky diagram for ECRIS performance.[1,38]

**TABLE I.** Main CB-ECRIS operating parameters.

| Support gas species | He |
|---|---|
| $P_{inj}$ (background) | $2.5 \times 10^{-8}$ mbar |
| $P_{inj}$ (operation) | $8.7 \times 10^{-8}$ mbar |
| Extraction voltage | 20 kV |
| Injected 1+ intensity | 710 nA |
| $B_{inj}$ | 1.58 T |
| $B_{min}$ | 0.45 T |
| $B_{ext}$ | 0.83 T |
| Microwave power | 500 W (14.5 GHz) |
| $\Delta V$ | −3.9 V |

**TABLE II.** The charge breeding efficiencies $\eta^q$ and the characteristic times obtained in Ref. 27. The relative uncertainties are computed from the absolute upper and lower uncertainty limits ($\hat{\delta}$ and $\check{\delta}$, respectively) according to $\delta = (\hat{\delta} + \check{\delta})/\tau$ for each $\tau$.

| Charge state | $\tau^q$ (ms) | $\delta$ (%) | $\tau^q_{inz}$ (ms) | $\delta$ (%) | $\tau^q_{cx}$ (ms) | $\delta$ (%) | $\eta^q$ (%) |
|---|---|---|---|---|---|---|---|
| 1 | ... | ... | ... | ... | ... | ... | 9.7 |
| 2 | ... | ... | ... | ... | ... | ... | 2.7 |
| 3 | ... | ... | ... | ... | ... | ... | 1.2 |
| 4 | ... | ... | ... | ... | ... | ... | 1.0 |
| 5 | $2.6^{+0.8}_{-0.4}$ | 46 | $2.6^{+0.5}_{-0.5}$ | 38 | $360^{+410}_{-250}$ | 183 | 1.1 |
| 6 | $2.6^{+1.7}_{-0.4}$ | 81 | $2.5^{+0.7}_{-0.7}$ | 56 | $26^{+26}_{-17}$ | 165 | 1.2 |
| 7 | $4^{+4}_{-2}$ | 150 | $2.6^{+0.9}_{-0.8}$ | 65 | $7^{+7}_{-4}$ | 157 | 1.5 |
| 8 | $7^{+10}_{-4}$ | 200 | $3.1^{+1.4}_{-0.8}$ | 71 | $4^{+5}_{-2}$ | 175 | 2.7 |
| 9 | $10^{+13}_{-4}$ | 170 | $10^{+4}_{-3}$ | 70 | $9^{+7}_{-3}$ | 111 | 8.9 |
| 10 | $16^{+19}_{-7}$ | 163 | $13^{+3}_{-4}$ | 54 | $13^{+15}_{-5}$ | 154 | 10.6 |
| 11 | ... | ... | ... | ... | ... | ... | 8.5 |
| 12 | ... | ... | ... | ... | ... | ... | 5.1 |
| | | | | | | | $\Sigma_q \eta^q = 54.2\,\%$ |

Importantly, we identified the EED as a possible source of error for the method. Although this is not directly reflected in the uncertainty bounds, it is used in the evaluation of the ionization rate coefficients and thus inherently affects the resultant $n_e$, $\langle E_e \rangle$ values. In the analysis in Ref. 27, the EED was presumed to be a simple Maxwell–Boltzmann (MB) distribution. Other error sources—including the support plasma perturbation—are discussed in Ref. 27 and in Appendix C.

We also found that the method yields considerable uncertainty bounds for the characteristic times. For high charge states, the relative uncertainty (68.2% confidence interval) of $\tau^q$ and $\tau^q_{cx}$ was >100 %. It was speculated that this uncertainty originates largely from the uncertainty of the ionization cross sections. In Ref. 27, the rate coefficients were obtained using the semi-empirical Voronov formula[39] and an umbrella uncertainty of 60% was applied to all charge states based on Ref. 39. This is incorrect as the uncertainty varies the charge state to charge state. Thereafter,[28,29] we have adopted the cross sections and the corresponding uncertainties from the semi-empirical formula and data reported in Refs. 30 and 36. We compute the rate coefficients using a chosen EED and apply each charge state the appropriate uncertainty as given in the literature. Understanding how the selection of the EED and the uncertainties of the ionization cross sections affect the results of the CT method (topic of this paper) can be considered a prerequisite for using the method in parametric studies of charge breeder ECRIS plasma parameters in upcoming measurement campaigns.

## III. ANALYSIS METHODS AND RESULTS

### A. Changing the EED

To study the effects of presuming different EEDs in computing the rate coefficients, we employed three different distributions: the default Maxwell–Boltzmann distribution, the kappa distribution,[40]

and a double Maxwell–Boltzmann distribution. Often, theoretical approaches in ECRIS physics employ the Maxwell–Boltzmann distribution. It presumes thermodynamic equilibrium in the ensemble of particles, which is not necessarily a rigorous assumption in the case of the non-equilibrium plasma of the ECRIS. The true EED remains unknown, but experimental measurements of the lost electron energy distribution (LEED) imply that the EED is non-Maxwellian.[14] In particular, there appears to exist a population of hot ∼100 keV electrons, which appear as a pronounced "hump" in the LEED.[15]

It is therefore interesting to investigate the effect of varying the high energy tail of the EED. The kappa distribution provides a mathematically convenient way to do this by varying the value of the spectral parameter $\kappa$, which has the effect of increasing the relative weight of the high energy tail as $\kappa$ decreases. For $\kappa \to \infty$, the kappa distribution approaches a Maxwell–Boltzmann distribution. The aforementioned LEED experiments, however, suggest that a double MB distribution might better describe the EED. We thus construct a double Maxwell–Boltzmann distribution with hot and warm electron populations, so that the hot population has a fixed $\langle E_e \rangle_h$ and the $\langle E_e \rangle_c$ is allowed to vary. This is justified as the ionization cross section is greater in the energy range corresponding to the warm electron population, and hence, the rate coefficient is more sensitive to variations of $\langle E_e \rangle_c$. The double MB distribution allows us to assign arbitrary fractions of the total electron population to either the warm or the hot population. We assume the EEDs to be isotropic although it could be argued that this does not hold for the hot electron population of the double MB distribution.

The Maxwell–Boltzmann distribution as a function of speed $v$ is

$$g(v) = \left(\frac{m}{2\pi kT}\right)^{3/2} 4\pi v^2 e^{-\frac{mv^2}{2kT}}, \tag{15}$$

where $k$ is the Boltzmann constant, $T$ is the temperature, and $m$ is the particle mass.

The kappa distribution was taken from Ref. 40 and converted to speed formalism by integrating over the solid angle in velocity space ($v^2 \mathrm{d}v\mathrm{d}\Omega$), which amounts to multiplication by $4\pi v^2$ thanks to the symmetry of the distribution. We have then

$$g_\kappa(v) = \frac{2v^2}{(\kappa w_\kappa^2)^{3/2}} \frac{\Gamma(\kappa+1)}{\Gamma(\kappa-1/2)\Gamma(3/2)} \left(1 + \frac{v^2}{\kappa w_\kappa^2}\right)^{-(\kappa+1)}, \tag{16}$$

where the thermal velocity $w_\kappa = \sqrt{(2\kappa-3)kT_{eq}/\kappa m}$, $T_{eq}$ is the so-called equivalent temperature, $\Gamma$ is the Gamma function, and the spectral index is $\kappa > 3/2$.

The double Maxwell–Boltzmann distribution was defined so that

$$g(v; \langle E_{e,c} \rangle) = n_e \left[ f_c g_c(v; \langle E_{e,c} \rangle) + f_h g_h(v; \langle E_{e,h} \rangle) \right], \tag{17}$$

where $g_h(v; \langle E_{e,h} \rangle)$ represents the hot electron population with a fixed average energy set to $\langle E_{e,h} \rangle = 100$ keV. The average energy of the warm population—the main provider of ionizing collisions—described by $g_c(v; \langle E_{e,c} \rangle)$ was allowed to vary. The coefficients $0\% \le f_c \le 100\%$ and $f_h = 100\% - f_c$ define the fraction of electrons assigned to the warm and hot population, respectively.

According to Ref. 41, switching off the microwave heating power leads to an abrupt 50% decrease in the electron flux escaping through the magnetic mirror. It was inferred that this occurs due to the elimination of rf-induced pitch angle scattering of electrons. The actual fractions of electrons in any given population are unknown, but since the rf-induced pitch angle scattering primarily affects the warm and hot electrons [with energies on the order of 10–100 keV (Ref. 41)], we infer that in the "worst-case-scenario" $f_h = 50\%$. In the following analysis, the hot population energy was set to $\langle E_e \rangle_h = 100$ keV. Another analysis was conducted with $\langle E_e \rangle_h = 200$ keV, but there were no significant deviations in the results.

To facilitate comparisons between the different EEDs, we use average energy of the distribution instead of the temperature or equivalent temperature. For the Maxwell–Boltzmann distribution, this amounts to the substitution $kT \to \frac{2}{3}\langle E_e \rangle$, but for the kappa distribution, we need to solve for a given $\langle E_e \rangle$,

$$\langle E_e \rangle = \int_0^\infty \left(\frac{1}{2}mv^2\right) g_\kappa(v; T)\mathrm{d}v \tag{18}$$

as a function of $T$, to obtain the equivalent temperature, which yields the desired $\langle E_e \rangle$. The rate coefficients are then computed according to Eq. (11) substituting the distributions from Eqs. (15), (16), and (17). Note that we use classical equations throughout the analysis.

Figure 2(a) plots the Maxwell–Boltzmann (MB) distribution together with the kappa distribution (for $\kappa = 2, 3, 5, 10$) as a function of the electron energy for a constant most probable energy of 2 keV. In Fig. 2(b), the MB distribution is compared to a double-Maxwellian distribution. In Fig. 2(b), the warm population most probable energy is fixed to 2 keV and the $\langle E_e \rangle_h = 100$ keV. The double-Maxwellian is plotted with different fractions of electrons assigned to the hot population, $f_h = 10\%, 20\%, 30\%, 40\%, 50\%$. The high energy behavior of the distributions is highlighted by the log–log inset plots. The particle number in each distribution is normalized, i.e., an integral over each distribution yields unity.

Figure 3 shows $\langle \sigma v \rangle^{\mathrm{inz,\,K}}_{8+\to 9+}$ with different EEDs as a function of $\langle E_e \rangle$. We observe that the maximum rate coefficient is reached at a higher $\langle E_e \rangle$ as $\kappa$ decreases. The double MB distribution on the other hand yields a flat low-$\langle E_e \rangle$ component to the rate coefficient at energies below 100 eV, thanks to the constant high energy population whose EED overlaps with a non-zero part of the ionization cross section. The small cross section at high energy is in part compensated by the large $v$. At high $\langle E_e \rangle$, the double MB distribution yields a smaller rate coefficient, because while the less energetic population approaches optimum energy, the contribution of the hot population remains constant.

Examples of the CT-method ($\langle E_e \rangle$,$n_e$) solution sets obtained using different EEDs are plotted for $K^{8+}$, $K^{9+}$, and $K^{10+}$ in Fig. 4. The contour encloses all bins for which the density of solutions is greater than 10% of the maximum. For lower values of $\kappa$, we find that the postdicted ($\langle E_e \rangle$, $n_e$) sets have shifted toward higher electron energy and density compared to the standard MB. In the case of the double MB EED, we find that a higher proportion of hot electrons reduces the $n_e$ domain at low $\langle E_e \rangle$—consistent with the higher rate coefficient in that region. In the high energy range, the double MB distribution yields nearly identical solutions as with the simple MB, which is to be expected as the rate coefficients deviate much less. For lower charge states ($K^{7+,6+,5+}$), the double MB distribution yields slightly higher $n_e$ values at low $\langle E_e \rangle$ than the standard MB. N.B. that we do not expect each charge state population to yield the same $n_e$ and $\langle E_e \rangle$ due to the spatial distribution of electrons as discussed in detail in Ref. 27.

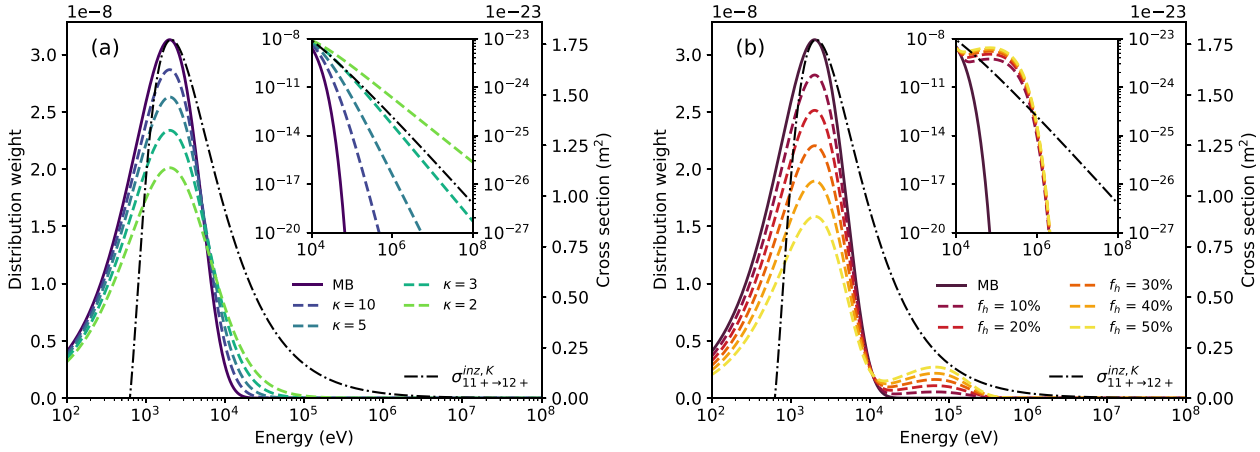


**FIG. 2.** Different EEDs plotted with a fixed most probable energy of 2 keV. The Maxwell–Boltzmann (MB) distribution and the kappa distribution for different values of $\kappa$ are plotted in subplot (a); the MB distribution and double-MB distribution with different assignments of electrons to the warm and hot populations are plotted in (b). In (a) $\kappa = 2, 3, 5, 10$ and in (b), the most probable energy of the warm population is fixed to 2 keV, while the fraction of electrons in the hot, 100 keV population gets values of $f_h = 10\%, 20\%, 30\%, 40\%, 50\%$. The ground state electron-impact ionization cross section $\sigma^{\text{inz, K}}_{11+\rightarrow 12+}$ is depicted by the black dashed line and is overlaid with the distributions. The insets highlight the high-energy behavior.

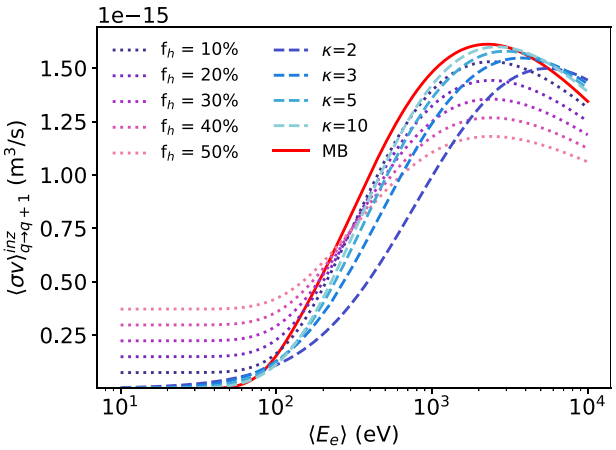


**FIG. 3.** $\langle \sigma v \rangle^{\text{inz}}_{8+\rightarrow 9+}$ for the reaction $e^- + K^{8+} \rightarrow K^{9+} + 2e^-$ as a function of $\langle E_e \rangle$ using different EEDs: Maxwell–Boltzmann (MB), kappa distribution ($\kappa = 2, 3, 5, 10$), and a double-Maxwellian distribution with the hot population fixed to $\langle E_e \rangle_h = 100$ keV and $f_h = 10\%, 20\%, 30\%, 40\%, 50\%$ of electrons assigned to the hot population.

Figure 5 shows the characteristic times as a function of the charge state obtained using different EEDs. The only major deviations are observed in the case of the confinement time of $K^{8+}$, $K^{9+}$, and $K^{10+}$. Both the double MB and kappa distribution results indicate that a presumed larger hot electron population postdicts a greater confinement time. The deviations remain within the uncertainty bounds, however. The similarity between the characteristic times obtained with the kappa distribution and a standard MB can be attributed to the similarity of the rate coefficients given by them (see Fig. 3). The double MB, on the other hand, has a significant contribution from the hot electron population even when the warm population has a moderate or low energy.

### B. Curtailing the cross section uncertainty

To investigate the effect of having more precise information of $\sigma^{\text{inz}}_{q\rightarrow q+1}$, we perform an artificial curtailment of its experimental uncertainty. Because the ionization rate coefficients directly inherit the uncertainty of the cross sections, the uncertainty of $\sigma^{\text{inz}}_{q\rightarrow q+1}$ is taken into account by repeating the $n_e, \langle E_e \rangle$ optimization multiple times ($\sim$1000) and adding a random bias to the rate coefficients $\langle \sigma v \rangle^{\text{inz}}_{q\rightarrow q+1}$ in each iteration. That is,

$$\langle \sigma v \rangle^{\text{inz}}_{q\rightarrow q+1} \rightarrow \langle \sigma v \rangle^{\text{inz}}_{q\rightarrow q+1}(\mathcal{A} + \mathcal{B}_q), \tag{19}$$

where $\mathcal{A}$ is a constant offset, and $\mathcal{B}_q$ is selected by a random, uniform sample from within the bounds of the experimental uncertainty of $\sigma^{\text{inz}}_{q\rightarrow q+1}$. Effectively, we limit the range from which $\mathcal{B}_q$ is sampled to a fraction of the reported uncertainty. Simultaneously, we vary the constant offset $\mathcal{A}$ to account for possible systematic errors in the cross section measurement. We constrain the selection of $\mathcal{A}$ and $\mathcal{B}_q$ so that the original uncertainty limits are never exceeded. As an example, if the added offset is 50% (i.e., $\mathcal{A} = 150\%$), then $\mathcal{B}_q \sim U(-50, 50)\% \times \delta\sigma^{\text{inz}}_{q\rightarrow q+1}$, where $U$ is the uniform distribution and is the largest extent of $\mathcal{B}_q$. Figure 6 shows the effect of varying the offset and the random bias. The different sets of $\mathcal{A}$ and $\mathcal{B}_q$ analyzed are tabulated in Table III.

Figure 7 shows the effect of curtailing the cross section (rate coefficient) uncertainty limits, with $K^{8+}$ used as an example case. The solution sets become progressively narrower as the uncertainty limits are tightened. The effect of decreasing $\mathcal{A}$ is to shift sets toward higher $n_e$. This is because the resulting lower value of $\langle \sigma v \rangle^{\text{inz}}$ needs to be compensated by a higher $n_e$, in order to obtain the ionization rate, which minimizes the penalty function [Eq. (10)]. Similar effects are seen for all charge states.

Figure 8 plots the characteristic times resulting from the curtailed solution sets. We can see that in general, the decreased uncertainty yields smaller uncertainty bounds. The characteristic times obtained for $K^{8+}$, which has the largest associated uncertainty of the cross section ($\delta\sigma^{\text{K,inz}}_{8+\rightarrow 9+} = 200\%$), from the different analyses are tabulated in Table IV.

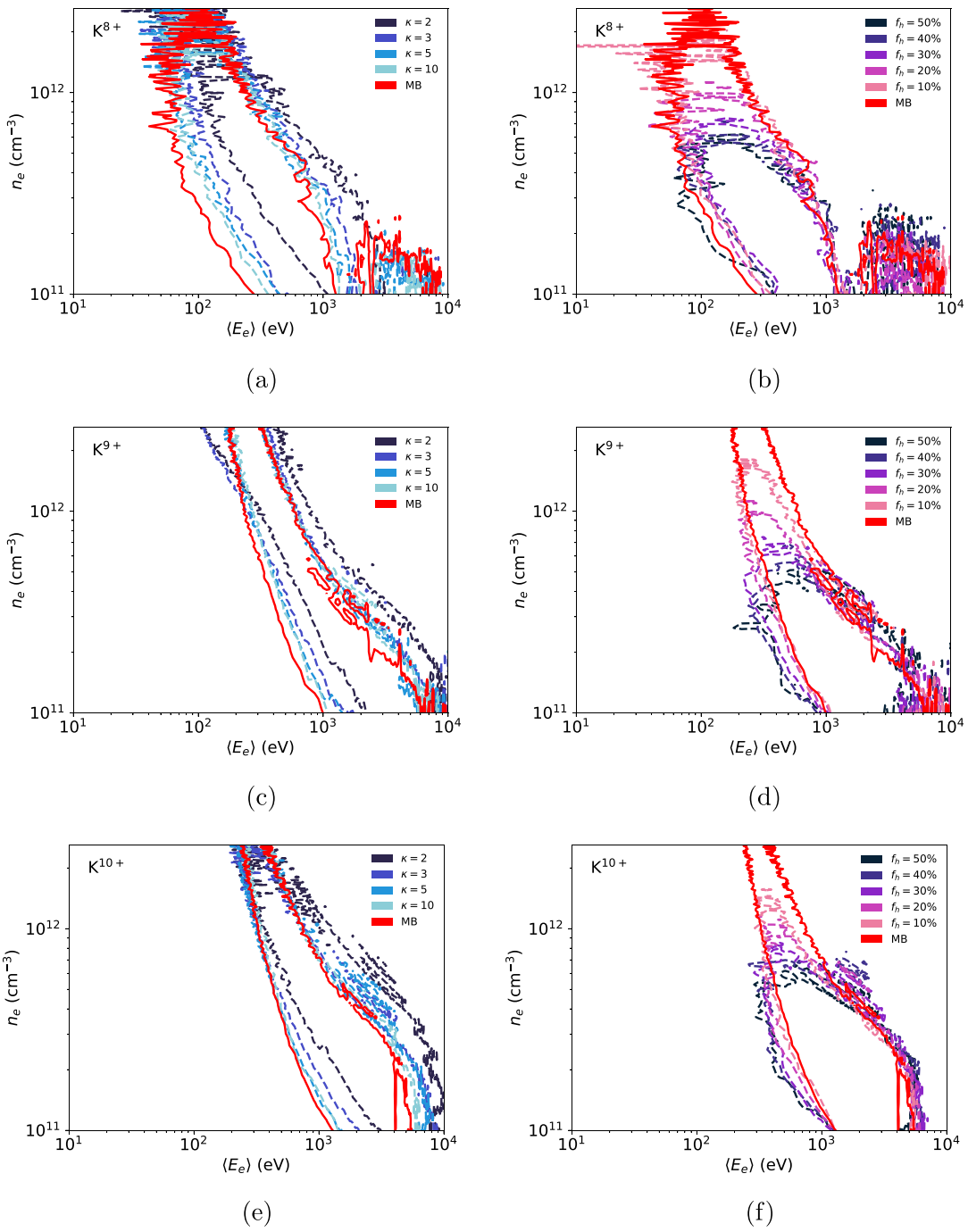


**FIG. 4.** Outer contours of the solution sets for $K^{8+}$, $K^{9+}$, and $K^{10+}$ with different EEDs. (a), (c), and (e) compare the results obtained with the kappa distributions, while (b), (d), and (f) show the sets obtained with the different double MB distributions. The standard MB distribution is plotted for reference in each figure. A Gaussian filter was applied to smooth the contours, improving legibility.

NB that the set 100–50 yields, counterintuitively, a greater uncertainty than the uncurtailed analysis. This happens when the decreased uncertainty range prohibits certain $\langle E_e \rangle$, $n_e$ values resulting in a greater variance in the resultant characteristic time distributions. In general, however, the curtailed uncertainty decreases the relative uncertainty of the characteristic times.

We note that the uncertainty of the confinement time of $K^{10+}$ increases across the board even though the uncertainty is decreased.

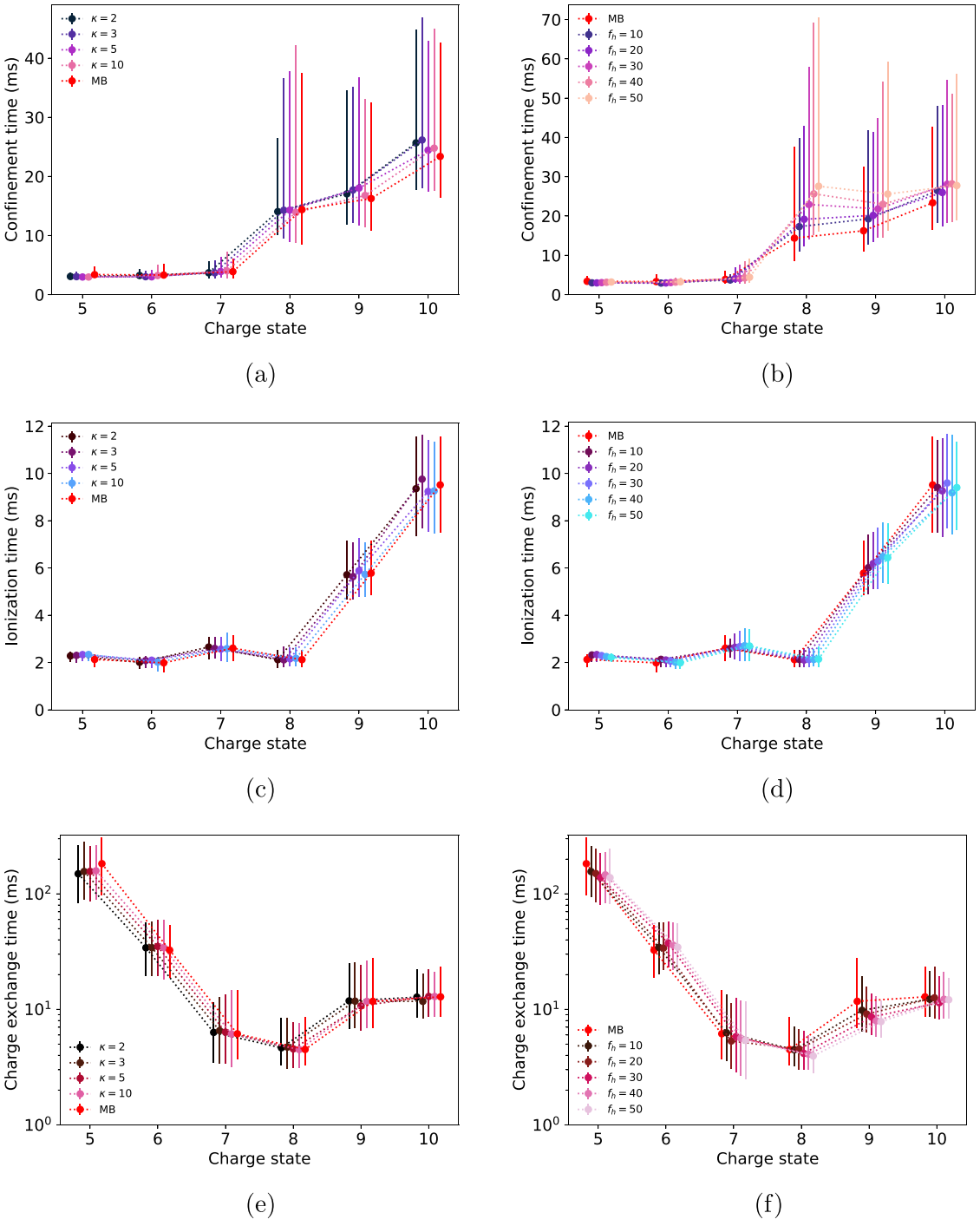


**FIG. 5.** The characteristic times of confinement, ionization, and charge exchange using different EEDs. (a), (c), and (e) plot solutions obtained using the kappa distribution, while (b), (d), and (f) plot solutions with the double MB distribution. The results for a standard MB distribution are plotted for reference in each subfigure.

Although the solution sets become narrower, they still cover a large swathe of the $\langle E_e \rangle$, $n_e$ space, which permits the broad distribution of $\tau^q$. That is, the remaining solutions in the solution set contain a great range of postdictions for $\tau^q$. In Appendix B, a further constraint on $n_e$ and $\langle E_e \rangle$ is shown to lead to the desired improved precision also for $K^{10+}$. Furthermore, we cannot rule out the low beam current of $K^{10+}$ from contributing to the seemingly counter-intuitive increase in the uncertainty.

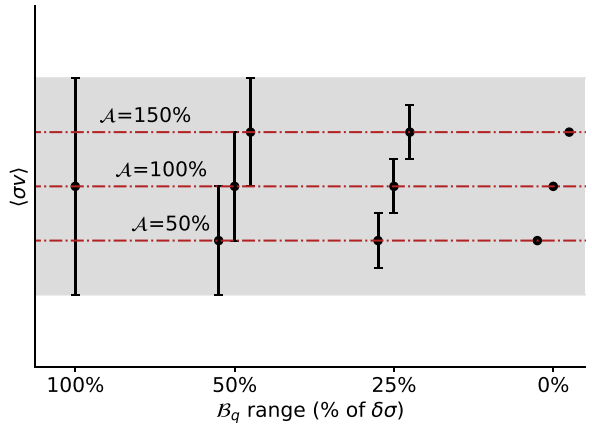


**FIG. 6.** Schematic illustration of artificially curtailing the rate coefficient/cross section uncertainty. The gray region shows the original experimental uncertainty. Applying the offset $\mathcal{A}$ shifts the center of $\langle\sigma v\rangle$, while curtailing the range of the random variable $\mathcal{B}_q$ narrows the uncertainty bounds. That is, $\mathcal{A}$ represents systematic error and $\mathcal{B}_q$ relative uncertainty.

**TABLE III.** The combinations of offset $\mathcal{A}$ and percentage range for the random bias $\mathcal{B}_q$ used in the analysis. The $\mathcal{B}_q$ is selected from a random uniform distribution as a percentage of the original uncertainty of the ionization cross section $\delta\sigma$. The combination $\mathcal{A} = 100\%$, $\mathcal{B}_q \sim U(0,0)\%$ corresponds to perfect knowledge of $\sigma^{\text{inz}}_{q\to q+1}$.

| Set label | $\mathcal{A}$ (%) | $\mathcal{B}_q$ (% × $\delta\sigma$) |
|---|---|---|
| 150-50 | 150 | $\sim U(-50,50)$ |
| 150-25 | 150 | $\sim U(-25,25)$ |
| 150-10 | 150 | $\sim U(-10,10)$ |
| 150-00 | 150 | $\sim U(0,0)$ |
| 100-50 | 100 | $\sim U(-50,50)$ |
| 100-25 | 100 | $\sim U(-25,25)$ |
| 100-10 | 100 | $\sim U(-10,10)$ |
| 100-00 | 100 | $\sim U(0,0)$ |
| 50-50 | 50 | $\sim U(-50,50)$ |
| 50-25 | 50 | $\sim U(-25,25)$ |
| 50-10 | 50 | $\sim U(-10,10)$ |
| 50-00 | 50 | $\sim U(0,0)$ |

## IV. DISCUSSION

### A. EED effects

The effect of the double MB distribution on the confinement time results is a consequence of the constant contribution from the hot electron population to the rate coefficients. Due to the presumed hot electron population, the high charge states' rate coefficient is many orders of magnitude greater than that computed using a single MB or kappa distribution, and the penalty function minimum is obtained at a lower $n_e$, which cuts off the high density region from the solution sets. Consequently, only a subset of characteristic time solutions is found using the double MB distribution as compared to the standard MB distribution (see Fig. 4).

The effect of varying $\kappa$ can also be seen in Fig. 4. Decreasing $\kappa$ causes the distribution to deviate more from the standard MB EED and to increase the relative weight of the high energy tail. Here, the differences at low energy are relatively less than that in the case of a double MB EED, and larger differences are seen at high $\langle E_e\rangle$. The resultant characteristic times are not affected significantly by the variation of $\kappa$.

### B. Curtailed uncertainty

It was observed that artificially reducing the uncertainty associated with the experimental values of $\sigma^{\text{inz}}_{q\to q+1}$ yields—in general—an improvement in the precision of the CT method results. The $(\langle E_e\rangle, n_e)$ solution sets become narrower, although they still trace a long path in the $(\langle E_e\rangle, n_e)$-space, i.e., we find a broad distribution of $(\langle E_e\rangle, n_e)$ pairs, which are consistent with the measured transient time series. We also obtain a concomitant improvement in the precision of the characteristic times, and the confinement and charge exchange times benefit the most, as evident from Table IV. The uncertainty, which remains after setting $\mathcal{B}_q \sim U(0,0)\%$, can be further reduced by a prior measurement of $\langle E_e\rangle$ and $n_e$, as indicated by the case study in Appendix B. These findings motivate a revisit of the electron impact ionization cross sections to improve their precision, and performing a measurement of $\langle E_e\rangle$ and/or $n_e$ in conjunction with the CT method experiments.

The most straightforward method for the determination of the electron density is probably through the combined bremsstrahlung emission and beam current spectroscopy—method expounded in Ref. 19. It requires, however, the EED to be known/presumed beforehand, as well as knowledge of the ion confinement times. In Ref. 19, the confinement times are assumed to be weakly dependent on $q$ based on findings in Ref. 34. $\tau^q$ found through the CT method implies that such an assumption underestimates the density of the high charge state ions, causing $n_e$ to be overestimated. Such an estimate could, however, be used as an upper limit for $n_e$. The bremsstrahlung detector should also be chosen so that the measurement is sensitive to the electron population with energy $\lesssim$1 keV, as the warm electron population is dominant in determining $\langle\sigma v\rangle^{\text{inz}}_{q\to q+1}$. Altogether, we identify simultaneous measurement of the bremsstrahlung emission (spectral temperature) and application of the CT method as the most straightforward method for reducing the uncertainty bounds of the obtained plasma parameters.

In Ref. 29, we showed that multi-species 1+ injection can also be used to reduce the uncertainty of the results. We used a composite Na/K pellet at the 1+ ion source, which produced $Na^+$ and $K^+$ ions via thermal emission, enabling us to switch between the two ion species without switching off the ECRIS, and hence to probe the same support plasma conditions with both 1+ ions. The high charge states of the two ions can be argued to originate from the same plasma volume, and an overlap of the respective solution sets is justified. Taking the overlap reduces the $\langle E_e\rangle$,$n_e$ space, leading to a reduction in the characteristic time uncertainties as well. For example, the uncertainties of $\tau^{9+}$, $\tau^{9+}_{\text{inz}}$, and $\tau^{9+}_{\text{cx}}$ for potassium were reduced by 40, 11, and 62 percentage points, respectively. This implies that better knowledge of the ionization cross section uncertainties could be expected to yield a more significant improvement. Despite the usefulness of the overlap method, it carries the weight of the additional assumption regarding the volume of origin of the ion populations, and only the high charge states benefit from it.

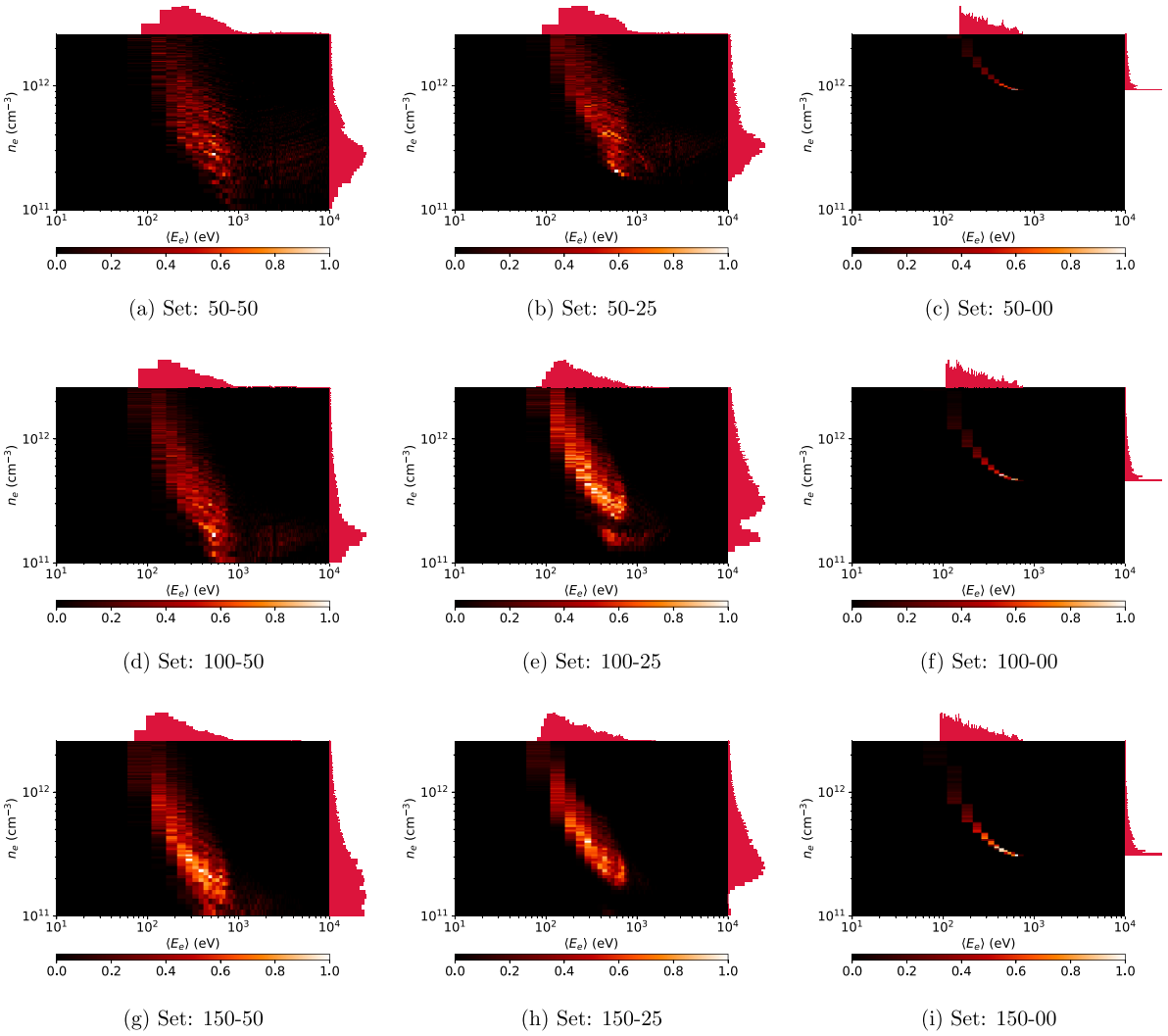


(a) Set: 50-50 (b) Set: 50-25 (c) Set: 50-00

(d) Set: 100-50 (e) Set: 100-25 (f) Set: 100-00

(g) Set: 150-50 (h) Set: 150-25 (i) Set: 150-00

**FIG. 7.** Solution sets for $K^{8+}$ using curtailed uncertainty ranges (denoted by the set number from Table III) and a simple Maxwell–Boltzmann EED.

### C. Conclusion

The effect of the EED on the CT method results can be summarized to arise from the modification of the $\langle \sigma v \rangle^{\mathrm{inz}}_{q \to q+1}$ it causes. The deviations in $\tau^q$, $\tau^q_{\mathrm{inz}}$, and $\tau^q_{\mathrm{cx}}$ due to the variation of the EED are well within the uncertainty bounds, but we expect that an increase in the precision of $\sigma^{\mathrm{inz}}_{q \to q+1}$ would show that the characterization of the EED is important in particular for determining $\tau^q$ of highly charged ions.

To determine the uncertainty originating from the EED in any real experimental setting, the experimenter should characterize the uncertainty related to their knowledge of the EED and test the effect on the results by varying the shape of the EED within the limits of that uncertainty (e.g., the fraction of electrons in the hot/warm population of a double MB distribution, or the precise value of $\kappa$ of a kappa distribution). The LEED measurement offers a route for the above, but the confined plasma EED may be different from the escaping one, as discussed in Ref. 15.

To our knowledge, the CT method is unique among ECRIS related plasma diagnostics, in that it accounts for the uncertainty of the electron-impact ionization cross section. The results in this work indicate that $\delta\sigma^{\mathrm{inz}}_{q \to q+1}$ has a significant effect on the CT method results' precision, and there is no reason to believe that other research, where the ionization cross sections are employed, would not be likewise affected. Its effects should thus be considered, for example, in simulations of the temporal evolution of the CSD in an ECRIS plasma (e.g., Refs. 10 and 12) and $k$–$\alpha$ measurements (e.g., Ref. 42). Such research would hence benefit greatly from a revisit of the cross sections—either through theoretical approaches or experimental measurement. We emphasize that the conclusion about the necessity of improved cross section data of high charge state electron impact ionization is not specific to potassium but would likewise reduce the uncertainty bounds for all 1+ probe beams (elements).

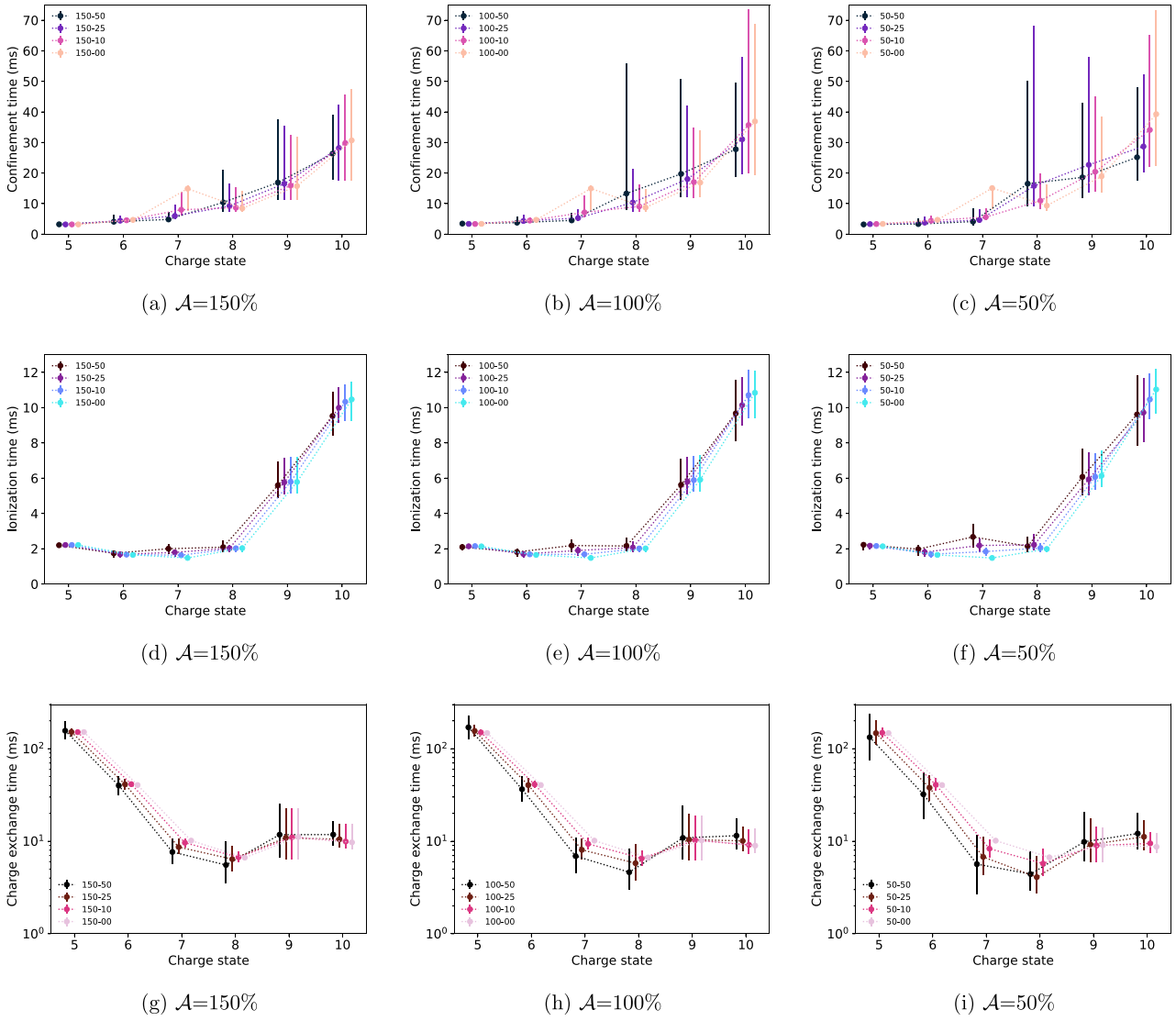


**FIG. 8.** Characteristic times using curtailed uncertainty ranges. Top row shows the confinement times, middle row the ionization times, and bottom row the charge exchange times. In each column, the offset $\mathcal{A}$ is fixed and the data points represent varying $\mathcal{B}_q$ range.

**TABLE IV.** The characteristic times of $K^{8+}$ and the corresponding relative uncertainties for different selections of $\mathcal{A}$ and $\mathcal{B}_q$. The uncurtailed set corresponds to full uncertainty range of $\sigma^{\mathrm{inz}}_{q\to q+1}$ and the sets 100-50, 100-25, 100-10, 100-00 to those tabulated in Table III. The relative uncertainties are computed from the absolute upper and lower uncertainty limits ($\hat{\delta}$ and $\check{\delta}$, respectively) according to $\delta = (\hat{\delta} + \check{\delta})/\tau$ for each $\tau$.

| Set | $\tau^q$ (ms) | $\delta$ (%) | $\tau^q_{\mathrm{inz}}$ (ms) | $\delta$ (%) | $\tau^q_{\mathrm{cx}}$ (ms) | $\delta$ (%) |
|---|---|---|---|---|---|---|
| Uncurtailed | $14.4^{+23.1}_{-5.9}$ | 200 | $2.1^{+0.4}_{-0.3}$ | 33 | $4.5^{+4.0}_{-1.2}$ | 120 |
| 100-50 | $13.3^{+42.3}_{-5.3}$ | 360 | $2.2^{+0.5}_{-0.3}$ | 34 | $4.6^{+3.7}_{-1.6}$ | 110 |
| 100-25 | $10.4^{+10.9}_{-2.9}$ | 130 | $2.1^{+0.4}_{-0.2}$ | 28 | $5.8^{+3.4}_{-2.1}$ | 100 |
| 100-10 | $9.1^{+7.3}_{-1.6}$ | 100 | $2.0^{+0.1}_{-0.2}$ | 16 | $6.5^{+1.5}_{-1.0}$ | 40 |
| 100-00 | $8.7^{+5.9}_{-1.4}$ | 80 | $2.0^{+0.1}_{-0.2}$ | 14 | $6.7^{+0.3}_{-0.1}$ | 6 |

## ACKNOWLEDGMENTS

We acknowledge grants of computer capacity from the Finnish Grid and Cloud Infrastructure (persistent identifier urn:nbn:fi:research-infras-2016072533) and support of the Academy of Finland Project funding (Grant No: 315855).

## AUTHOR DECLARATIONS

### Conflict of Interest

The authors have no conflicts to disclose.

### Author Contributions

**Miha Luntinen:** Conceptualization (equal); Data curation (lead); Formal analysis (lead); Methodology (equal); Project administration (lead);

Software (lead); Validation (lead); Visualization (lead); Writing – original draft (lead); Writing – review & editing (lead). **Julien ANGOT:** Conceptualization (equal); Formal analysis (supporting); Investigation (lead); Methodology (equal); Writing – original draft (supporting); Writing – review & editing (supporting). **Hannu Koivisto:** Conceptualization (equal); Formal analysis (supporting); Funding acquisition (equal); Project administration (supporting); Supervision (equal); Writing – original draft (supporting); Writing – review & editing (supporting). **Olli Tarvainen:** Conceptualization (equal); Data curation (supporting); Formal analysis (supporting); Project administration (supporting); Supervision (equal); Writing – original draft (supporting); Writing – review & editing (supporting). **Thomas Thuillier:** Formal analysis (supporting); Funding acquisition (equal); Project administration (supporting); Resources (lead); Supervision (equal); Writing – original draft (supporting); Writing – review & editing (supporting). **Ville Toivanen:** Data curation (supporting); Formal analysis (supporting); Funding acquisition (equal); Project administration (supporting); Resources (lead); Supervision (equal); Writing – original draft (supporting); Writing – review & editing (supporting).

## DATA AVAILABILITY

The data that support the findings of this study are openly available in figshare at https://doi.org/10.6084/m9.figshare.13602827.v1, Ref. 43. The analysis codes employed in this work are openly available in GitHub at https://github.com/misapema-jyfl/ct-analyzer (Release: ct-analyzer-v2.0), Ref. 44. The cross section curtailment was performed on a customized version of the released code, which is available upon reasonable request from the corresponding author.

## APPENDIX A: PENALTY FUNCTION UPPER LIMIT VARIATION AND NUMBER OF SOLUTIONS WITH CURTAILED CROSS SECTIONS

The number of solutions in a given data set is plotted as a function of the upper limit of the penalty function of Eq. (10), F, in Fig. 9. The value $F \leq 10^{-6}$ ensures that sufficient statistics are obtained for each solution set, while at the same time eliminating sources of crude error. The figure shows the number of solutions only for Maxwellian EED as similar behavior was found regardless of the assumed EED, i.e., $F \leq 10^{-6}$ was deemed appropriate in each case. Figure 10 shows the solution set of $K^{10+}$ for using different upper limits of $F$. It can be seen that requiring smaller values of $F$ rarefies the solution set uniformly in $(\langle E_e \rangle, n_e)$-space, i.e., valid results are found throughout the optimization bounds.

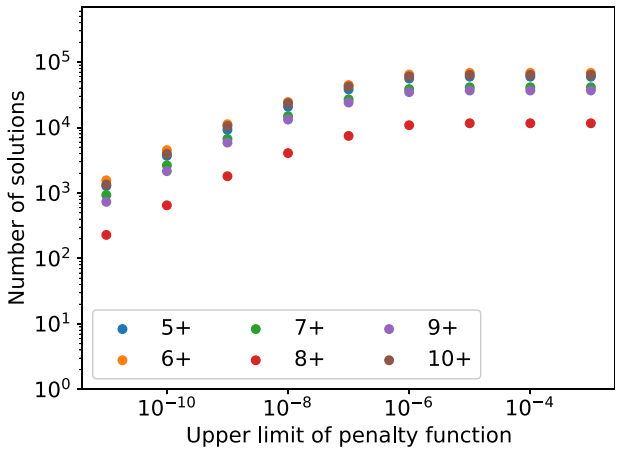


**FIG. 9.** The number of solutions in the solution sets obtained for different charge states as a function of the upper limit of the penalty function. The plot corresponds to data from the data set using a single Maxwell–Boltzmann EED.

In addition to the penalty function value, the number of solutions in $(\langle E_e \rangle, n_e)$-space is affected by the choice of the offset $\mathcal{A}$ and random bias $\mathcal{B}_q$ used in the analysis. As an example, Table V lists the number of solutions for $K^{8+}$ (assuming Maxwellian EED), i.e., the case presented in Fig. 7, when $\mathcal{A}$ and $\mathcal{B}_q$ are varied. We observe that (i) the number of solutions decreases as $\mathcal{A}$ is decreased keeping $\mathcal{B}_q$ constant, and (ii) the number of solutions increases as $\mathcal{B}_q$ is decreased keeping $\mathcal{A}$ constant. We associate (i) with the shift of the solutions in the $(\langle E_e \rangle, n_e)$-space, in particular fewer solutions are found at high $n_e$ when $\mathcal{A}$ is decreased. There is no apparent reason for (ii) other than the decrease in the number of "pathological" (unphysical) solutions outside the allowed $(\langle E_e \rangle, n_e)$-domain with decreasing $\mathcal{B}_q$. Altogether the number of solutions is always significant (9000–19 000 for $K^{8+}$, even higher for other charge states), which guarantees statistical significance of the analysis.

## APPENDIX B: CURTAILING THE SOLUTION SET RANGE

It was found that the curtailment of the ionization cross section uncertainty led to a broadening of the error estimate for the confinement time of $K^{10+}$. Therefore, in addition to the artificial curtailment of the cross section uncertainty, we performed a case study on $K^{10+}$ where we imposed further (arbitrary) limitations also on the $\langle E_e \rangle$ and $n_e$ values. This was done in the post-processing phase on the solution sets obtained for both an uncurtailed analysis using the standard MB EED, and the set 100–00 ($\mathcal{A} = 100\%$ and $\mathcal{B}_q \sim U(0, 0)$ %, i.e., presumed perfect knowledge of the $\sigma^{\text{inz}}_{q \to q+1}$). This extra analysis simulates the hypothetical effect of having a more precise knowledge of the plasma conditions prior to applying the CT method. The limitation on the $\langle E_e \rangle$ and $n_e$ values was applied as shown in Fig. 11. We select solutions from a region in $(\langle E_e \rangle, n_e)$-space so that $\langle E_e \rangle \in [1, 2]$ keV, and $n_e \in [1, 2] \times 10^{11}$ $\text{cm}^{-3}$—plotted in the figure in cyan. Table VI tabulates the results. It can be seen that decreasing $\delta\sigma^{\text{inz}}_{q \to q+1}$ and applying the further constraint on the density and average energy yields a considerable decrease in the uncertainty of $\tau^q$, which goes from the 117% of the standard, non-limited MB set, to the 30% for the limited set 100-00. On the other hand, merely limiting either the $\delta\sigma^{\text{inz}}_{q \to q+1}$ or the $\langle E_e \rangle$, $n_e$ values does not appear to be as effective in the case of $K^{10+}$. The $\tau^q_{\text{inz}}$ and $\tau^q_{\text{cx}}$ also benefit from the additional limitation on the solution set ranges.

## APPENDIX C: THE EFFECT OF THE 1+ PULSE LENGTH

The reliability of the characteristic times obtained with the CT method is subject to uncertainties other than the intrinsic ones discussed in detail in this paper. In particular, the potential perturbation caused by the 1+ injection is a relevant concern. The level of

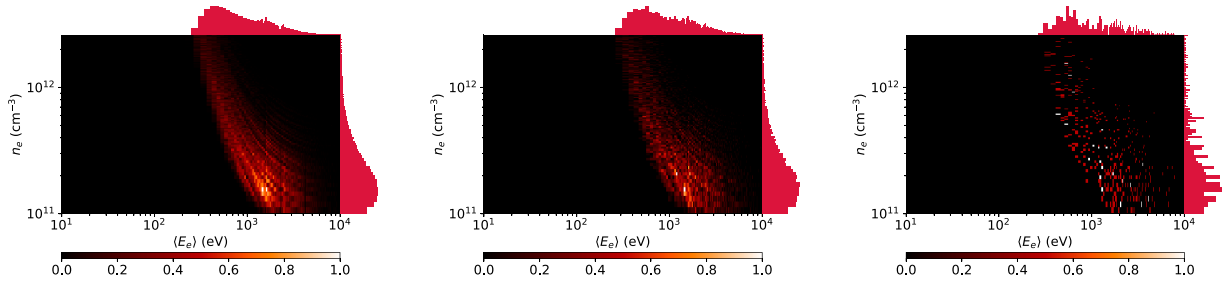


(a) $F < 1 \times 10^{-6}$ (b) $F < 1 \times 10^{-9}$ (c) $F < 1 \times 10^{-12}$

**FIG. 10.** The effect of varying the upper limit of the penalty function value on the solution set obtained for $K^{10+}$.

**TABLE V.** The number of $(\langle E_e \rangle, n_e)$-solutions for $K^{8+}$ for various $\mathcal{A}$ and $\mathcal{B}_q$ with Maxwellian EED. The corresponding solution spaces are illustrated in Figs. 7(a)–7(i).

| $\mathcal{A}$-$\mathcal{B}_q$ | Number of solutions | Figure |
|---|---|---|
| 50-50 | 9420 | 7(a) |
| 50-25 | 11 933 | 7(b) |
| 50-00 | 14 358 | 7(c) |
| 100-50 | 14 293 | 7(d) |
| 100-25 | 16 832 | 7(e) |
| 100-00 | 17 574 | 7(f) |
| 150-50 | 15 543 | 7(g) |
| 150-25 | 18 344 | 7(h) |
| 150-00 | 18 758 | 7(i) |

the charge breeder plasma perturbation is proportional to the number of injected particles, i.e., the 1+ beam current (see Ref. 16) and the length of the 1+ beam pulse. The pulse length is more relevant for the CT method as it profoundly affects the shape of the high charge state beam current transients and, thus, the resulting fitting parameters $a_q$, $b_q$, and $c_q$. The usable pulse length is limited by two factors: (a) The 1+ pulse needs to be long enough to ensure the intensities of the highest charge state ions ($K^{10+}$ in our case) are sufficiently above the noise level of the measurement, and (b) the 1+ pulse needs to be shorter than the saturation time of the high charge state ion signals (often referred to as the breeding time) to preserve the transient nature of the measurement and to avoid excessive perturbation of the charge breeder plasma. These two conditions render the 1+ beam pulse duration, $t_{1+}$ to be in the range of $5\,\text{ms} \leq t_{1+} \leq 100\,\text{ms}$ as found through a series of experiments. In this range, the 1+ beam pulse length does not affect the results, namely, the characteristic times, obtained with the CT method, i.e., the characteristic times computed from the data at different 1+ pulse lengths are within the uncertainty resulting from the cross section data. This is demonstrated in Fig. 12 where the confinement,

**TABLE VI.** The characteristic time results for $K^{10+}$ using a Maxwell–Boltzmann EED without curtailing the cross section uncertainty (MB); with cross section uncertainty curtailed to $\mathcal{A} = 100\%$ and $\mathcal{B}_q \sim U(0,0)$ (set 100-00); and with their ranges limited to $\langle E_e \rangle \in [1,2]$ keV, $n_e \in [1,2] \times 10^{11}$ cm$^{-3}$ (limited MB and limited set 100-00, respectively). The relative uncertainties are computed from the absolute upper and lower uncertainty limits ($\hat{\delta}$ and $\check{\delta}$, respectively) according to $\delta = (\hat{\delta} + \check{\delta})/\tau$ for each $\tau$.

| Set | $\tau^q$ (ms) | $\delta$ (%) | $\tau^q_{\text{inz}}$ (ms) | $\delta$ (%) | $\tau^q_{\text{cx}}$ (ms) | $\delta$ (%) |
|---|---|---|---|---|---|---|
| MB | $23^{+20}_{-7}$ | 117 | $10^{+2}_{-2}$ | 40 | $13^{+11}_{-5}$ | 123 |
| 100-00 | $37^{+32}_{-18}$ | 135 | $9^{+5}_{-2}$ | 78 | $11^{+2}_{-2}$ | 36 |
| Limited MB | $36^{+31}_{-11}$ | 116 | $12^{+2}_{-2}$ | 33 | $9^{+2}_{-2}$ | 44 |
| Limited 100-00 | $46^{+8}_{-6}$ | 30 | $11^{+1}_{-1}$ | 18 | $8^{+1}_{-1}$ | 25 |

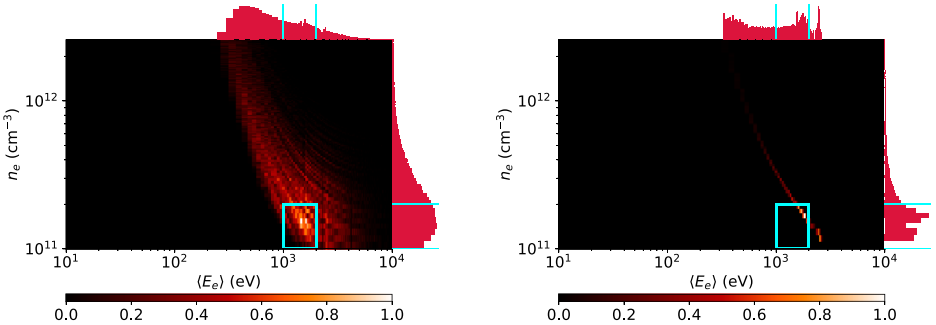


(a) (b)

**FIG. 11.** The solution sets for $K^{10+}$ using a Maxwell–Boltzmann EED with the default uncertainty ranges (a) and using arbitrary curtailed uncertainty (from set 100-00) (b). The region $n_e \in [1,2] \times 10^{11}$ cm$^{-3}$ and $\langle E_e \rangle \in [1,2]$ keV is highlighted in cyan.

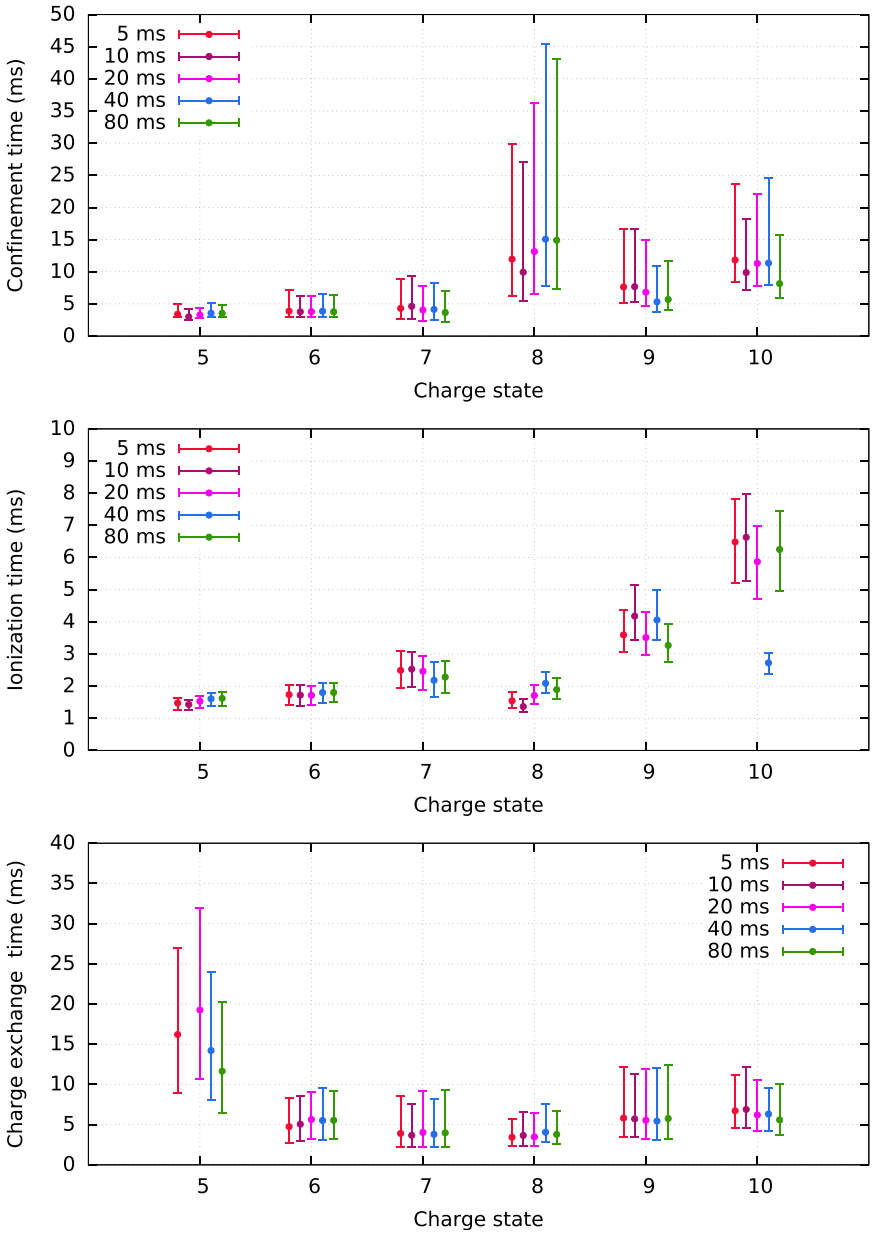


**FIG. 12.** Confinement times, ionization times, and charge exchange times of potassium charge states from 5+ to 10+ with varied pulse length of the injected 1+ beam.

ionization, and charge exchange times of potassium (charge states 5+ to 10+) are plotted at five different 1+ beam pulse lengths ranging from 5 to 80 ms. It is evident that the results are within the uncertainty bounds with a single exception of the ionization time of $K^{10+}$ at 40 ms 1+ pulse length, which we attribute to experimental error. Here, we note that the data with varying 1+ pulse length were recorded at a different time from the data discussed in the main text of this paper and hydrogen ($H_2$) was used as a buffer gas instead of helium. The choice of the buffer gas does not change the conclusion that within the above limits of the 1+ pulse length, the uncertainties related to the EED and ionization cross section are greater than those arising from the experiment itself.

## REFERENCES

[1]R. Geller, *Electron Cyclotron Resonance Ion Sources and ECR Plasmas* (Institute of Physics Publishing, Bristol/Philadelphia, 1996).
[2]R. Geller, T. Lamy, and P. Sortais, "Charge breeding of isotope on-line-created radioactive ions using an electron cyclotron resonance ion trap," Rev. Sci. Instrum. **77**, 03B107 (2006).
[3]Y. Blumenfeld, T. Nilsson, and P. V. Duppen, "Facilities and methods for radioactive ion beam production," Phys. Scr. **2013**, 014023.
[4]A. Kitagawa, T. Fujita, M. Muramatsu, S. Biri, and A. G. Drentje, "Review on heavy ion radiotherapy facilities and related ion sources (invited)," Rev. Sci. Instrum. **81**, 02B909 (2010).
[5]A. Kitagawa, T. Fujita, and M. Muramatsu, "Present status and future prospect of heavy ion radiotherapy," in *Proceedings of the 23rd International Workshop*

*on ECR Ion Sources (ECRIS'18), International Workshop on ECR Ion Sources No. 23* (JACoW Publishing, Geneva, Switzerland, 2019), pp. 49–52.
[6]S. Biri, R. Racz, J. Palinkas, C. Hegedus, and S. Kokenyesi, "Application of the ATOMKI-ECRIS for materials research," J. Electr. Electron. Eng. **2**, 113–116 (2009), see https://www.researchgate.net/publication/288730015_Application_of_the_ATOMKI-ECRIS_for_materials_research.
[7]T. Uchida, H. Minezaki, K. Tanaka, M. Muramatsu, T. Asaji, Y. Kato, A. Kitagawa, S. Biri, and Y. Yoshida, "Bio-nano ECRIS: An electron cyclotron resonance ion source for new materials production," Rev. Sci. Instrum. **81**, 02A306 (2010).
[8]F. J. C. Wenander, "Charge breeding of radioactive ions," in *Comments: 30 Pages, Contribution to the CAS-CERN Accelerator School: Ion Sources* edited by R. Bailey (CERN, Senec, Slovakia, 2013).
[9]A. Galatà, D. Mascali, L. Neri, and L. Celona, "A new numerical description of the interaction of an ion beam with a magnetized plasma in an ECR-based charge breeding device," Plasma Sources Sci. Technol. **25**, 045007 (2016).
[10]V. Mironov, S. Bogomolov, A. Bondarchenko, A. Efremov, and V. Loginov, "Numerical model of electron cyclotron resonance ion source," Phys. Rev. Spec. Top.-Accel. Beams **18**, 1–23 (2015).
[11]V. Mironov, S. Bogomolov, A. Bondarchenko, A. Efremov, V. Loginov, and D. Pugachev, "Spatial distributions of plasma potential and density in electron cyclotron resonance ion source," Plasma Sources Sci. Technol. **29**, 065010 (2020).
[12]G. Shirkov, "A classical model of ion confinement and losses in ECR ion sources," Plasma Sources Sci. Technol. **2**, 250–257 (1993).
[13]V. P. Pastukhov, "Classical longitudinal losses of plasma in open adiabatic traps," Voprosy Teor. Plaz. **16**(13), 160–204 (1984) (Russian), see https://inis.iaea.org/search/search.aspx?orig_q=RN:16082553.
[14]I. Izotov, O. Tarvainen, V. Skalyga, D. Mansfeld, T. Kalvas, H. Koivisto, and R. Kronholm, "Measurement of the energy distribution of electrons escaping minimum-B ECR plasmas," Plasma Sources Sci. Technol. **27**, 025012 (2018).
[15]I. Izotov, O. Tarvainen, V. Skalyga, D. Mansfeld, H. Koivisto, R. Kronholm, V. Toivanen, and V. Mironov, "Measurements of the energy distribution of electrons lost from the minimum B-field-the effect of instabilities and two-frequency heating," Rev. Sci. Instrum. **91**, 013502 (2020).
[16]O. Tarvainen, T. Lamy, J. Angot, T. Thuillier, P. Delahaye, L. Maunoury, J. Choinski, L. Standylo, A. Galatà, G. Patti, and H. Koivisto, "Injected 1+ ion beam as a diagnostics tool of charge breeder ECR ion source plasmas," Plasma Sources Sci. Technol. **24**, 035014 (2015).
[17]O. Tarvainen, T. Kalvas, H. Koivisto, J. Komppula, R. Kronholm, J. Laulainen, I. Izotov, D. Mansfeld, V. Skalyga, V. Toivanen, and G. Machicoane, "Limitation of the ECRIS performance by kinetic plasma instabilities (invited)," Rev. Sci. Instrum. **87**, 02A703 (2016).
[18]D. Mascali, E. Naselli, and G. Torrisi, "Microwave techniques for electron cyclotron resonance plasma diagnostics," Rev. Sci. Instrum. **93**, 033302 (2022).
[19]A. Gumberidze, M. Trassinelli, N. Adrouche, C. I. Szabo, P. Indelicato, F. Haranger, J.-M. Isac, E. Lamour, E.-O. Le Bigot, J. Mérot, C. Prigent, J.-P. Rozet, and D. Vernhet, "Electronic temperatures, densities, and plasma x-ray emission of a 14.5 GHz electron-cyclotron resonance ion source," Rev. Sci. Instrum. **81**, 033303 (2010).
[20]C. Barué, M. Lamoureux, P. Briand, A. Girard, and G. Melin, "Investigation of hot electrons in electron-cyclotron-resonance ion sources," J. Appl. Phys. **76**, 2662–2670 (1994).
[21]J. Noland, O. Tarvainen, J. Benitez, D. Leitner, C. Lyneis, and J. Verboncoeur, "Studies of electron heating on a 6.4 GHz ECR ion source through measurement of diamagnetic current and plasma bremsstrahlung," Plasma Sources Sci. Technol. **20**, 035022 (2011).
[22]R. C. Pardo, R. Harkewicz, and P. J. Billquist, "Time evolution of charge states in an electron cyclotron resonance ion source," Rev. Sci. Instrum. **67**, 1602–1605 (1996).
[23]M. Imanaka, T. Nakagawa, H. Arai, I. Arai, and S. M. Lee, "Plasma diagnostics of liquid He-free SC-ECR ion source (SHIVA) with use of laser ablation technique," Nucl. Instrum. Methods Phys. Res., Sect. B **237**, 647–655 (2005).
[24]D. Neben, J. Fogleman, D. Leitner, G. Machicoane, G. Parsey, A. Pham, S. Renteria, J. Stetson, L. Tobos, and J. Verboncoeur, "Fast sputtering measurement studies using uranium with the NSCL ECR ion sources," in *Proceedings of the ECRIS'16* (JACoW Publishing, Geneva, Switzerland, 2016), pp. 128–132.
[25]D. E. Neben, G. Machicoane, A. N. Pham, J. W. Stetson, G. Parsey, and J. P. Verboncoeur, "An analysis of fast sputtering studies for ion confinement time," in *Proceedings of the LINAC'16* (JACoW Publishing, Geneva, Switzerland, 2016), pp. 475–477.
[26]M. Marttinen, J. Angot, A. Annaluru, P. Jardin, T. Kalvas, H. Koivisto, S. Kosonen, R. Kronholm, L. Maunoury, O. Tarvainen, V. Toivanen, and P. Ujic, "Estimating ion confinement times from beam current transients in conventional and charge breeder ECRIS," Rev. Sci. Instrum. **91**, 013304 (2020).
[27]J. Angot, M. Luntinen, T. Kalvas, H. Koivisto, R. Kronholm, L. Maunoury, O. Tarvainen, T. Thuillier, and V. Toivanen, "Method for estimating charge breeder ECR ion source plasma parameters with short pulse 1+ injection of metal ions," Plasma Sources Sci. Technol. **30**, 035018 (2021).
[28]M. Luntinen, J. Angot, O. Tarvainen, V. Toivanen, T. Thuillier, and H. Koivisto, "Measurement of ionization, charge exchange and ion confinement times in charge breeder ECR ion sources with short pulse 1+ injection of metal ions," J. Phys.: Conf. Ser. **2244**, 012009 (2022).
[29]M. Luntinen, V. Toivanen, H. Koivisto, J. Angot, T. Thuillier, O. Tarvainen, and G. Castro, "Diagnostics of highly charged plasmas with multicomponent 1+ ion injection," Phys. Rev. E **106**, 055208 (2022).
[30]M. A. Lennon, K. L. Bell, H. B. Gilbody, J. G. Hughes, A. E. Kingston, M. J. Murray, and F. J. Smith, "Recommended data on the electron impact ionization of atoms and ions: Fluorine to nickel," J. Phys. Chem. Ref. Data **17**, 1285–1363 (1988).
[31]A. Müller and E. Salzborn, "Scaling of cross sections for multiple electron transfer to highly charged ions colliding with atoms and molecules," Phys. Lett. A **62**, 391–394 (1977).
[32]H. Knudsen, H. K. Haugen, and P. Hvelplund, "Single-electron capture by highly charged ions colliding with atomic and molecular hydrogen," Phys. Rev. A **24**, 2287–2290 (1981).
[33]R. Kronholm, T. Kalvas, H. Koivisto, J. Laulainen, M. Marttinen, M. Sakildien, and O. Tarvainen, "Spectroscopic study of ion temperature in minimum-B ECRIS plasma," Plasma Sources Sci. Technol. **28**, 075006 (2019).
[34]G. Douysset, H. Khodja, A. Girard, and J. P. Briand, "Highly charged ion densities and ion confinement properties in an electron-cyclotron-resonance ion source," Phys. Rev. E **61**, 3015–3022 (2000).
[35]G. D. Shirkov, "Calculation of ion charge-state distribution in ECR ion sources," Technical Report No. UCRL-53391 (Lawrence Livermore National Laboratory, 1982).
[36]K. L. Bell, H. B. Gilbody, J. G. Hughes, A. E. Kingston, and F. J. Smith, "Recommened data on the electron impact ionization of light atoms and ions," J. Phys. Chem. **12**, 891–916 (1983).
[37]We note here that in Ref. 27 the equation of $\tau_{cx}^{q}$ has a typographical error, but the correct equation was implemented in the numerical analysis and the results were not affected.
[38]K. S. Golovanivsky, Instrum. Exp. Tech. **28**, 989 (1986).
[39]G. Voronov, "A practical fit formula for ionization rate coefficients of atoms and ions by electron impact: Z = 1–28," At. Data Nucl. Data Tables **65**, 1–35 (1997).
[40]V. Pierrard and M. Lazar, "Kappa distributions: Theory and applications in space plasmas," Sol. Phys. **267**, 153–174 (2010).
[41]M. Sakildien, O. Tarvainen, R. Kronholm, I. Izotov, V. Skalyga, T. Kalvas, P. Jones, and H. Koivisto, "Experimental evidence on microwave induced electron losses from ECRIS plasma," Phys. Plasmas **25**, 062502 (2018).
[42]M. Sakildien, O. Tarvainen, T. Kalvas, H. Koivisto, R. Kronholm, R. Thomae, J. Mira, F. Nemulodi, and P. Jones, "Investigation into the gas mixing effect in ECRIS plasma using kα and optical diagnostics," AIP Conf. Proc. **2011**, 040010 (2018).
[43]J. Angot and M. Luntinen, "Consecutive_transients_sample_data," Figshare (2021), see https://doi.org/10.6084/m9.figshare.13602827.v1.
[44]M. Luntinen, "Consecutive transients analyzer," GitHub (2023), version 2.0; see https://github.com/misapema-jyfl/ct-analyzer.